Available online at www.sciencedirect.com
SCIENCE DIRECT®
Journal of Solid State Chemistry 177 (2004) 3514–3521
JOURNAL OF SOLID STATE CHEMISTRY
http://elsevier.com/locate/jssc

Crystal structure and phase transitions of strontium zirconium diorthophosphate, $SrZr(PO_4)_2$

Koichiro Fukuda*, Akira Moriyama, Shinobu Hashimoto

Department of Environmental and Materials Engineering, Nagoya Institute of Technology, Gokiso-cho, Showa-ku, Nagoya-shi, Aichi-ken 466-8555, Japan

Received 4 January 2004; received in revised form 12 April 2004; accepted 2 June 2004

Available online 11 August 2004

Abstract

The crystal structure of $SrZr(PO_4)_2$ at 298 K was determined from conventional X-ray powder diffraction data using direct methods, and it was further refined by the Rietveld method. The structure was triclinic (space group $P\bar{1}$, $Z = 2$) with $a = 0.77508(4)$ nm, $b = 0.78887(5)$ nm, $c = 0.51251(3)$ nm, $\alpha = 95.754(3)°$, $\beta = 90.228(2)°$, $\gamma = 92.474(2)°$, and $V = 0.31149(3)$ nm^3. Final reliability indices were $R_{wp} = 8.51\%$, $R_p = 6.07\%$, and $R_B = 2.46\%$. The powder specimens were also examined by high-temperature XRD and differential thermal analysis to reveal the occurrence of phase transitions from triclinic to monoclinic at 405 K, then to hexagonal (or trigonal) at 1196 K during heating. Upon cooling, the reverse change of the latter transition occurred at 1175 K. The subsequent monoclinic-to-triclinic transition was martensitic and incomplete during further cooling to 298 K. The monoclinic phase is most probably isostructural with yavapaiite. The present paper has described, for the first time, the higher- and lower-temperature polymorphs of the yavapaiite-type structure.

Keywords: Strontium zirconium diorthophosphate; Phase transitions; High-temperature XRD; Rietveld method

1. Introduction

Zirconium phosphates are among the most promising materials for catalysts, ion exchangers, and ion conductors. The compounds $AZr(PO_4)_2$ with A = Ba, Sr and Ca were successfully prepared in previous studies [1–6]. The $BaZr(PO_4)_2$ crystal is most probably isostructural with yavapaiite ($KFe(SO_4)_2$) as judged by the complete similarity in both powder XRD and vibrational patterns of IR and Raman spectra [1,2]. The compound $SrZr(PO_4)_2$ was supposed to be related to the yavapaiite-type structure; however, it showed more complicated X-ray pattern [4]. The crystal structure of $CaZr(PO_4)_2$ was determined in our proceeding paper, showing the distinction from the yavapaiite-type structure [6].

In the present study, we have determined the crystal structure of $SrZr(PO_4)_2$ from powder XRD data using direct methods. The powder specimens were further examined at high temperatures to demonstrate the occurrence of phase transitions.

2. Experimental

2.1. Synthesis

The present specimen of strontium zirconium diorthophosphate $SrZr(PO_4)_2$ was prepared from stoichiometric amounts of reagent-grade chemicals $SrCO_3$, ZrO_2, and $NH_4H_2PO_4$. A mixture of the former two chemicals was first heated at 1773 K for 1 h in order to synthesize the crystals of $SrZrO_3$. Then, the product was mixed with the latter. The mixture was pressed into pellets (12 mm diameter and 3 mm thick), heated at 1573 K for 100 h, followed by quenching in air. The sintered pellets consisting of the $SrZr(PO_4)_2$ crystals were spontaneously pulverized during the cooling process. This suggests that the crystals under-

*Corresponding author. Fax: +81-52-735-5289.
E-mail address: fukuda.koichiro@nitech.ac.jp (K. Fukuda).

0022-4596/$ - see front matter © 2004 Elsevier Inc. All rights reserved.
doi:10.1016/j.jssc.2004.06.002

went the phase transitions that must be accompanied by tensile deformations.

2.2. Crystal structure determination

X-ray powder diffraction intensities for structural determination were collected at 298 K on a PANalytical X'Pert diffractometer in Bragg–Brentano geometry using monochromatized Cu$K\alpha$ radiation (50 kV, 40 mA) and a step-scan technique in a 2θ range from 10° to 149.98° with a fixed counting time (t) of 15 s/step and a step interval ($\Delta 2\theta$) of 0.02°. Peak positions were determined after $K\alpha_2$ stripping on a computer program POWDERX [7], followed by the indexing procedure on a computer program TREOR90 [8]. In the latter procedure, 2θ values of 35 peak positions were used as input data. Only one triclinic cell was found with satisfactory figures of merit $M_{20}/F_{20} = 45/73(0.007297, 38)$, $M_{30}/F_{30} = 24/41(0.007809, 0)$, and $M_{35}/F_{35} = 17/30(0.008829, 133)$ [9,10]. The derived unit-cell parameters, $a = 0.77493(7)$ nm, $b = 0.78846(12)$ nm, $c = 0.51235(7)$ nm, $\alpha = 95.76(1)°$, $\beta = 90.209(9)°$, and $\gamma = 92.48(2)°$, were subsequently used as starting parameters in the next stage of the analysis.

Table 1
Crystal data of strontium zirconium diorthophosphate

Chemical composition	$SrZr(PO_4)_2$
Space group	$P\bar{1}$
a (nm)	0.77508(4)
b (nm)	0.78887(5)
c (nm)	0.51251(3)
α (deg)	95.754(3)
β (deg)	90.228(2)
γ (deg)	92.474(2)
V (nm^3)	0.31149(3)
Z	2
D_x ($Mg\,m^{-3}$)	3.93

Profile intensity data for refinement of unit-cell parameters were collected in a 2θ range from 10° to 70° with $t = 5$ s/step. Si powder was used as an internal standard reference material ($SrZr(PO_4)_2$/Si = 4 in weight). The unit-cell parameters were refined by the whole powder-pattern decomposition method, based on the Pawley algorithm [11], on a computer program WPPF [12]. The systematic peak shift $\Delta(2\theta)$ was corrected with the function $\Delta(2\theta) = t_0 + t_1 \cos 2\theta + t_2 \sin 2\theta$. During the decomposition process, the parameters $t_0 - t_2$ were refined together with the unit-cell parameters, while the unit-cell parameter of Si was fixed at a value of $a = 0.5430825$ nm [13]. The refined unit-cell parameters (Table 1) could index all reflections in the observed diffraction pattern.

Both of the possible space groups $P1$ and $P\bar{1}$ were tested using the EXPO package [14] for crystal structure determination. The lower reliability index R_F [15] of 18.1% was obtained with the latter space group in a default run of the program. Structural parameters of all atoms were refined by the Rietveld method on a computer program RIETAN [16] using the profile intensity data in the 2θ range of $20.5 - 149.98°$ (Fig. 1). The total number of reflections were 1240. The background intensities were fitted to a polynomial function with 12 adjustable parameters. The pseudo-Voigt function [17] was used to fit the peak profile. The systematic peak shift $\Delta(2\theta)$ was corrected with the function $\Delta(2\theta) = t_0 + t_1 \cos 2\theta + t_2 \sin 2\theta + t_3 \tan\theta$, while the unit-cell parameters were fixed throughout the refinement process. The preferred-orientation parameter of March–Dollase function [18], r, was refined to be $r = 0.854(1)$ with the preferred-orientation vector [100], suggesting that the crystals were fractured along

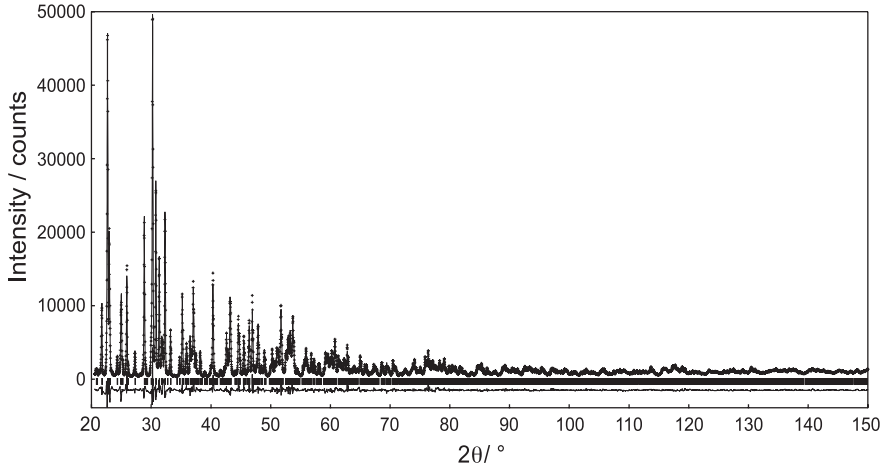

Fig. 1. Comparison between observed (+marks) and calculated (upper solid line) patterns of strontium zirconium diorthophosphate. The difference curve is shown in the lower part of the figure. Vertical marks indicate the positions of possible Bragg reflections.

Table 2
Structural parameters of strontium zirconium diorthophosphate, $SrZr(PO_4)_2$

Atom	x	y	z	B (nm^2)
Sr	0.4771(1)	0.2300(2)	0.3025(3)	0.0064(4)
Zr	0.9742(1)	0.2770(1)	0.3391(2)	0.0018(3)
P1	0.7507(4)	0.3741(5)	0.7855(8)	0.0023(7)
P2	0.7862(4)	0.8766(5)	0.1998(8)	0.0052(8)
O1	0.7568(8)	0.204(1)	0.591(1)	0.002(1)
O2	0.5807(8)	0.455(1)	0.735(1)	0.002(1)
O3	0.7766(9)	0.329(1)	0.080(1)	0.006(1)
O4	0.9137(8)	0.461(1)	0.683(1)	0.004(1)
O5	0.5974(9)	0.923(1)	0.191(1)	0.002(1)
O6	0.8172(8)	0.772(1)	0.449(1)	0.003(1)
O7	0.8377(8)	0.766(1)	0.951(1)	0.003(1)
O8	0.9205(9)	0.027(1)	0.223(1)	0.014(2)

the distinct cleavage planes parallel to (100). Isotropic thermal parameters, B, were assigned to all atoms. Reliability indices for a final result were $R_{wp} = 8.51\%$, $R_p = 6.07\%$ and $R_B = 2.46\%$ [15]. Crystal data are given in Table 1, and final positional and thermal parameters of atoms are given in Table 2.

2.3. Thermal behavior

The thermal behavior was investigated up to 1473 K by a differential thermal analysis (DTA, Model TG8120, Rigaku Co., Tokyo, Japan). The temperature was controlled by a Pt–PtRh (10%) thermocouple, with heating and cooling rates of 10 K/min. The phase constitution as well as changes in cell parameters were examined by XRD equipped with a heating stage. The profile data with $t = 2$ s/step were collected in the 2θ range from 10° to 60° during stepwise heating up to 1473 K (step width = ~100 K) and subsequent cooling down to 298 K. Powder specimens, mixed with Au powder as an internal temperature standard [19], were deposited with ethyl alcohol on the platinum heating filament ($132 \times 9 \times 1$ mm^3). A programmable divergence slit was employed to maintain an illumination length of 10 mm on the sample. Thus an illumination area of 10×9 mm^2 was realized regardless of the 2θ value. The cell parameters were refined by the WPPD method [12].

3. Results and discussion

3.1. Structure description

Fig. 2 shows a structure fragment of strontium zirconium diorthophosphate. Selected interatomic distances and bond angles, together with their standard uncertainties, are listed in Table 3. Valence bond sums (Table 4) calculated on the basis of bond-strength analysis [20,21] are in good agreement with expected

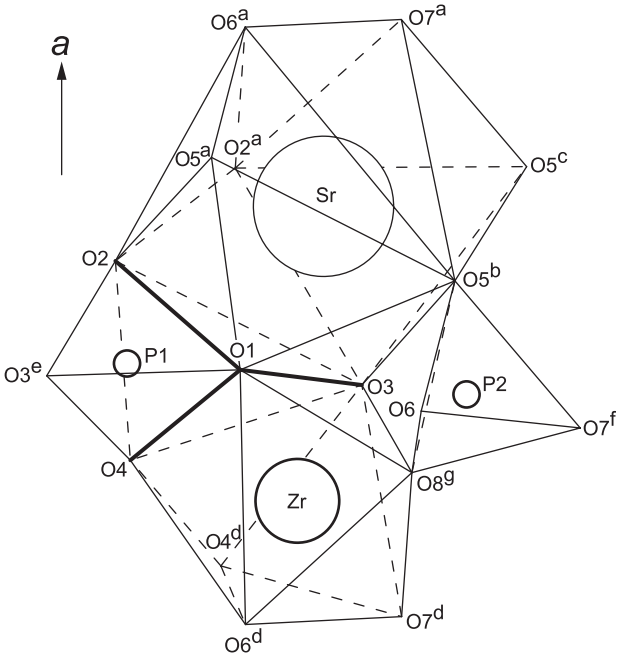

Fig. 2. Part of the structure viewed along [0 1 $\bar{1}$]. Atom numbering corresponds to that given in Table 2. Labels a, b, c, d, e, f, and g correspond to the symmetry transformations in Table 3.

formal oxidation states of Sr^{2+}, Zr^{4+}, P^{5+}, and O^{2-} ions. Distortion parameters for the coordination polyhedra (Table 5) were determined using a computer program IVTON [22].

The mean P1–O and P2–O bond lengths in the PO_4 tetrahedra (respectively, 0.156 and 0.155 nm) are in good agreement with those expected from the bond valence sum (0.152 nm). The mean values of the O–P–O angles are 109° for both tetrahedra. These values are in good agreement with those found in other orthophosphates [23].

The Zr atom is sevenfold coordinated, as in the other known zirconium orthophosphates $Zr_2O(PO_4)_2$ [24] and $CaZr(PO_4)_2$ [6]. The mean Zr–O distance is 0.213 nm, which is comparable to those of the ZrO_7 polyhedron in $Zr_2O(PO_4)_2$ (0.2143 nm) and $CaZr(PO_4)_2$ (0.216 nm). Ratio of volumes of the circumscribed sphere and the polyhedron (V_S/V_P) for the ZrO_7 is 2.765 (Table 5). Because the V_S/V_P value of the ideal pentagonal bipyramid is 2.643 [25], the present ZrO_7 can be described as a distorted pentagonal bipyramid. The Sr atom is coordinated to nine oxygen atoms, forming a tricapped trigonal prism. A similar geometry around the Sr atom has been described in strontium lithium borate, $SrLiB_9O_{15}$. [26]. In the crystal structure, the SrO_9 polyhedron showed the bond lengths ranging from 0.271 to 0.284 nm (the mean = 0.277 nm).

Ionic radii of Sr^{2+} in the ninefold coordination [$r(Sr^{2+}(9)) = 0.131$ nm and $r(O^{2-}(8)) = 0.142$ nm] and that of Zr^{4+} in the sevenfold coordination [$r(Zr^{4+}(7)) = 0.078$ nm and $r(O^{2-}(6)) = 0.140$ nm] pre-

Table 3
Coordinates of Sr, Zr, and P

	O1	O2	O2[a]	O3	O5[b]	O5[c]	O5[a]	O6[a]	O7[a]
Sr									
O1	0.2645(7)	54.8(2)	110.4(2)	65.4(2)	71.2(2)	128.2(2)	66.8(2)	116.1(2)	172.5(2)
O2	0.251(1)	0.2790(8)	64.7(4)	86.0(2)	124.4(2)	165.3(2)	68.8(2)	82.7(2)	124.3(2)
O2[a]	0.428(1)	0.288(1)	0.2570(9)	80.1(2)	160.0(3)	103.2(2)	119.9(2)	84.4(2)	73.6(2)
O3	0.289(1)	0.375(1)	0.340(1)	0.2711(7)	82.8(2)	83.6(2)	132.1(2)	163.6(2)	122.0(2)
O5[b]	0.308(1)	0.481(1)	0.514(1)	0.354(1)	0.2645(8)	64.4(3)	79.6(3)	113.4(2)	107.4(2)
O5[c]	0.485(1)	0.549(1)	0.416(1)	0.363(1)	0.287(1)	0.2740(8)	125.8(3)	105.2(2)	54.9(2)
O5[a]	0.313(1)	0.329(1)	0.484(1)	0.523(1)	0.363(1)	0.513(1)	0.3015(9)	53.4(2)	105.8(2)
O6[a]	0.447(1)	0.357(1)	0.348(1)	0.527(1)	0.440(1)	0.426(1)	0.255(1)	0.2617(7)	57.3(2)
O7[a]	0.540(1)	0.4910(1)	0.320(1)	0.479(1)	0.436(1)	0.254(1)	0.461(1)	0.258(1)	0.2762(7)
	O1	O3	O4	O4[d]	O6[d]	O7[d]	O8		
Zr									
O1	0.2217(7)	84.0(3)	63.0(3)	126.1(3)	102.7(3)	155.3(3)	75.4(3)		
O3	0.289(1)	0.2106(8)	99.7(3)	89.0(3)	173.1(3)	95.6(3)	86.7(3)		
O4	0.232(1)	0.332(1)	0.2232(8)	65.9(4)	85.1(3)	140.7(3)	136.6(3)		
O4[d]	0.396(1)	0.304(1)	0.242(1)	0.2222(8)	88.5(3)	78.5(3)	157.5(3)		
O6[d]	0.3308(9)	0.412(1)	0.288(1)	0.296(1)	0.2017(7)	77.6(3)	93.1(3)		
O7[d]	0.422(1)	0.312(1)	0.408(1)	0.274(1)	0.258(1)	0.2099(8)	79.9(3)		
O8	0.260(1)	0.284(1)	0.396(1)	0.417(1)	0.294(1)	0.265(1)	0.2029(9)		
	O1	O2	O3[e]	O4					
P1									
O1	0.1592(8)	107.1(5)	109.4(4)	96.1(4)					
O2	0.251(1)	0.1521(8)	114.4(5)	116.4(5)					
O3[e]	0.260(1)	0.262(1)	0.1596(9)	111.6(5)					
O4	0.232(1)	0.2595(9)	0.259(1)	0.1531(8)					
	O5	O6	O7[f]	O8[g]					
P2									
O5	0.1524(8)	109.1(5)	111.9(5)	116.3(5)					
O6	0.255(1)	0.161(1)	108.5(5)	106.2(5)					
O7[f]	0.254(1)	0.256(1)	0.1537(9)	104.4(5)					
O8[g]	0.260(1)	0.252(1)	0.243(1)	0.1537(9)					

The values in diagonals are the central atom–ligand distances (nm), in the upper right triangle the bond angles (deg), and in the lower left the ligand–ligand distances (nm) are given.
Symmetry transformations used to generate equivalent atoms: a: $1-x$, $1-y$, $1-z$; b: x, $-1+y$, z; c: $1-x$, $1-y$, $-z$; d: $2-x$, $1-y$, $1-z$; e: x, y, $1+z$; f: x, y, $-1+z$; g: x, $1+y$, z.

Table 4
Bond valence calculations

	Sr	Zr	P1	P2	V_i
O1	0.24	0.47	1.03		1.7
O2	0.16		1.25		
O2	0.29				}1.7
O3	0.20	0.63	1.02		1.9
O4		0.45	1.22		
O4		0.46			}2.1
O5	0.24			1.24	
O5	0.19				}1.8
O5	0.09				
O6	0.26	0.81		0.98	2.1
O7	0.18	0.65		1.20	2.0
O8		0.78		1.20	2.0
V_i	1.9	4.2	4.5	4.6	

$V_i = \sum_j \exp[(R_{ij} - d_{ij})/b]$ with $b = 0.037$ nm and $R_{ij} = 0.2118$ nm for Sr^{2+}, 0.1937 nm for Zr^{4+}, and 0.1604 nm for P^{5+}.

Table 5
Polyhedral distortion parameters

Polyhedron	Distortion parameters				
	Δ (nm)	r_s (nm)	V_S (nm^3)	σ	V_P (nm^3)
SrO_9	0.020	0.272	0.0862	0.957	0.0362
ZrO_7	0.012	0.213	0.0411	0.977	0.0149
$P1O_4$	0.006	0.156	0.0159	1	0.0019
$P2O_4$	0.006	0.155	0.0157	1	0.0019

Δ = eccentricity; r_s = radius of sphere fitted to ligands; V_S = sphere volume; σ = sphericity; V_P = volume of coordination polyhedron; σ for coordination number four is 1 by definition.

dict the interatomic distances of 0.273 nm for Sr–O and 0.218 nm for Zr–O [27]. These predicted values are in good agreement with the corresponding mean inter-

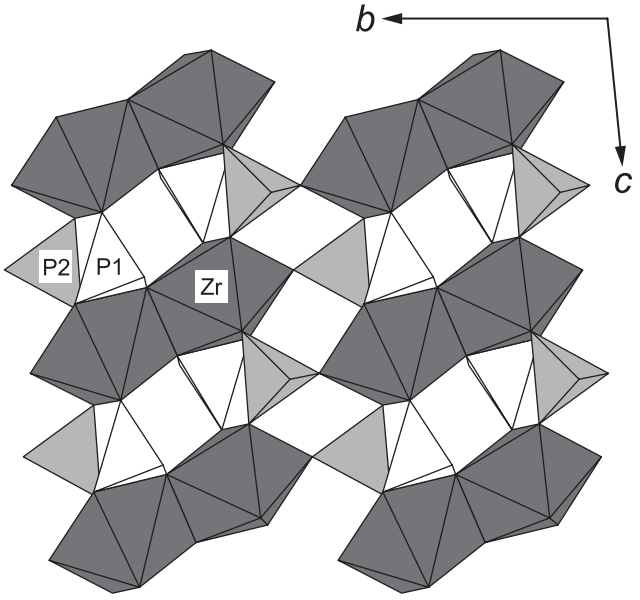

Fig. 3. Projection of part of the structure along the *a*-axis. Two of the Zr coordination polyhedra mutually share edges, and they are connected through $P1O_4$ and $P2O_4$ polyhedra to form infinite chains parallel to [001]. Individual chains are linked together with formation of a two-dimensional sheet parallel to (100).

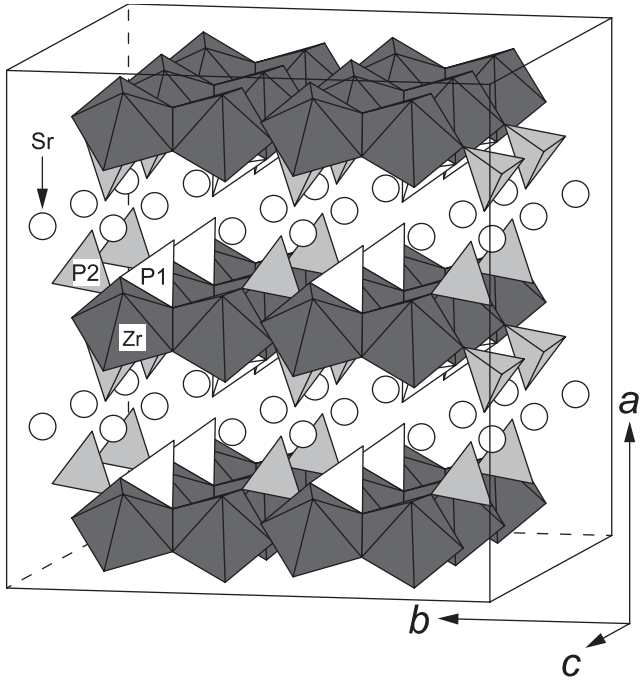

Fig. 4. Crystal structure of strontium zirconium diorthophosphate.

atomic distances of $\langle SrO\rangle = 0.272$ nm and $\langle ZrO\rangle = 0.213$ nm. The mean interatomic distances are also in accordance with those expected from the bond valence sum (0.267 nm for Sr–O and 0.214 nm for Zr–O).

The crystal structure of strontium zirconium diorthophosphate consists of the four types of polyhedra, SrO_9, ZrO_7, $P1O_4$, and $P2O_4$. Two of the Zr coordination polyhedra mutually share O4–O4^d edges, and they are connected through $P1O_4$ and $P2O_4$ polyhedra to form infinite chains running parallel to [001]. Individual chains are linked via oxygen atoms O8 of the $P2O_4$ and ZrO_7 polyhedra, resulting in the formation of a two-dimensional sheet parallel to (100) in Fig. 3. These sheets are stacked in the [100] direction, and they are linked through the strontium atoms to form a three-dimensional structure (Fig. 4).

3.2. Phase transitions during heating and cooling

The high-temperature XRD showed that there existed two other phases (Fig. 5). During the heating process up to 394 K, the crystal was exclusively composed of the triclinic phase. At temperatures 504–1173 K, the peak positions and their intensities were very similar to those of $BaZr(PO_4)_2$ [2], which is isostructural with yavapaiite (space group $C2/m$). The refined cell parameters could index all reflections in the observed diffraction patterns. For the profile intensity data taken above 1273 K, all of the reflections were successfully indexed on a hexagonal unit cell. The refined cell parameters are, for example, at 1473 K, $a = 0.51440(3)$ nm, $c = 0.76731(5)$ nm, and $V = 0.17583(2)$ nm^3 with the possible crystal system being hexagonal or trigonal. The two endothermic effects of DTA at 405 and 1196 K during heating were, therefore, assigned as the phase transitions from triclinic to monoclinic, then to hexagonal (or trigonal), respectively. Upon cooling, the reverse phase transition of the latter occurred at temperatures between 1273 and 1173 K. The exothermic effect of DTA at 1175 K during cooling would be due to this transition. At 1073–504 K, the sample was exclusively composed of the monoclinic phase. The subsequent monoclinic-to-triclinic transition was incomplete, hence both phases coexisted below 394 K.

The probable lattice correspondences among the three polymorphs are:

$$\begin{bmatrix}\mathbf{a}_m\\ \mathbf{b}_m\\ \mathbf{c}_m\end{bmatrix} = \begin{bmatrix}0 & 1 & 0\\ 0 & 0 & 1\\ 1 & 0 & 0\end{bmatrix}\begin{bmatrix}\mathbf{a}_t\\ \mathbf{b}_t\\ \mathbf{c}_t\end{bmatrix}$$

and

$$\begin{bmatrix}\mathbf{a}_h\\ \mathbf{b}_h\\ \mathbf{c}_h\end{bmatrix} = \begin{bmatrix}1 & \bar{1} & 0\\ 1 & 0 & 0\\ 0 & 0 & 1\end{bmatrix}\begin{bmatrix}\mathbf{a}_m\\ \mathbf{b}_m\\ \mathbf{c}_m\end{bmatrix},$$

where $\mathbf{a}_t$, $\mathbf{b}_t$, and $\mathbf{c}_t$ are the lattice vectors of the triclinic phase, $\mathbf{a}_m$, $\mathbf{b}_m$, and $\mathbf{c}_m$ are those of the monoclinic phase, and $\mathbf{a}_h$, $\mathbf{b}_h$, and $\mathbf{c}_h$ are those of the hexagonal phase. The

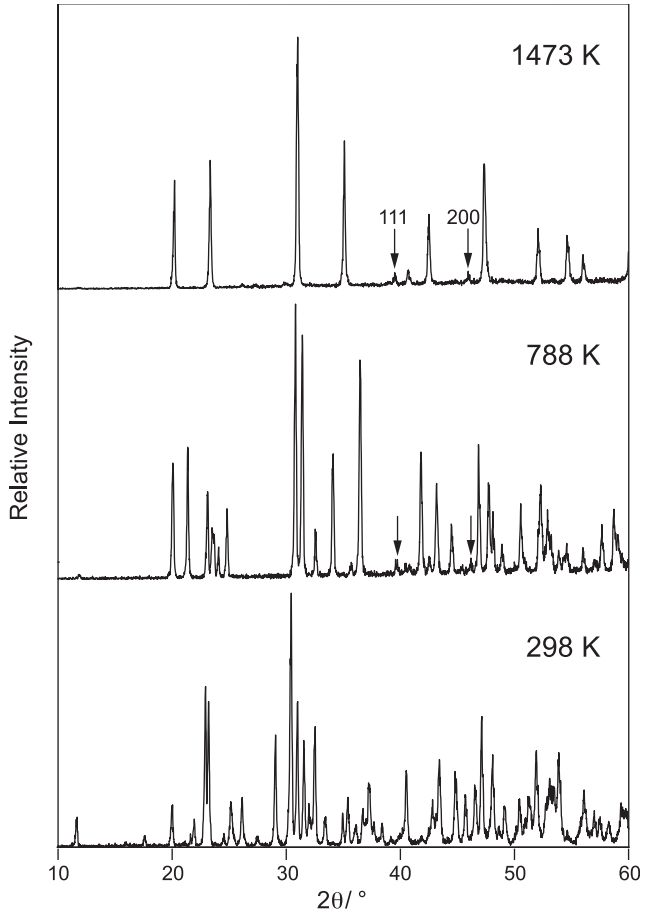

Fig. 5. Changes in powder XRD pattern induced by the two-phase transitions from triclinic to monoclinic, then to hexagonal (or trigonal) during heating from 298 to 1473 K. Arrows indicate the positions of 111 and 200 reflections with the platinum heating filament.

c_m-axis and $(001)_m$, for example, become the a_t-axis and $(100)_t$, respectively.

The changes in cell dimensions with increasing and decreasing temperature are, together with the transition temperatures, shown in Fig. 6. The triclinic-to-monoclinic phase transition during heating was accompanied by an increase in unit-cell volume by $\sim 6\%$; the b_t- and c_t-axis expanded by ~ 6 and $\sim 3\%$, respectively, and the a_t-axis shrank by $\sim 3\%$. Accordingly, during the reverse (monoclinic-to-triclinic) transition, the parent crystal would one dimensionally expand nearly along the c_m-axis, while volumetrically contract by $\sim 6\%$. This lattice deformation would generate a relatively large tensile stress nearly along the c_m-axis, which could result in the formation of micro-cracking parallel to $(001)_m$ and eventually cause the disintegration of the crystal grains. This speculation is strongly supported by the probable cleavage planes of the fractured crystals, being parallel to $(100)_t$.

When the powder specimen was cooled from high temperatures, the monoclinic phase remained at ambient temperature. On the other hand, for the sintered pellet samples, it was completely inverted to the triclinic phase during cooling. These imply that the internal thermal stress effectively promotes the phase transition, as in the case of martensitic transformations [28]. Accordingly, the monoclinic-to-triclinic phase transition could be martensitic.

To our knowledge, no other phase transition has been reported in crystals with the yavapaiite-type structure. The triclinic structure determined in the present study can be described as the lower-temperature polymorph of the yavapaiite-type structure. The space group change from $C2/m$ to its subgroup $P\bar{1}$ eliminates the twofold axis parallel to b_m, the mirror perpendicular to b_m, and the translation $\frac{1}{2}(\mathbf{a}_m + \mathbf{b}_m)$. The order of point group reduces from 4 (point group $2/m$) to 2 ($\bar{1}$), and the number of lattice points per unit cell reduces from 2 (C-centered lattice) to 1 (primitive). Thus, the number of variants possible to produce during the phase transition is $4[=(4\times 2)/(2\times 1)]$ [29]. These variants are pseudo-merohedral and antiphase that are related by the lost symmetry operations. For the crystal with the higher-temperature polymorph, the structural determination will be a future subject. A detailed comparison of the atomic arrangements among the three polymorphs would enhance our understanding of the crystal chemistry of the yavapaiite-related compounds.

4. Conclusion

We determined the crystal structure of $SrZr(PO_4)_2$ at 298 K, being triclinic with space group $P\bar{1}$. The Sr atom is ninefold coordinated, and Sr atom and surrounding oxygen atoms form a tricapped trigonal prism with a mean Sr–O distance of 0.272 nm. The ZrO_7 coordination polyhedron is a distorted pentagonal bipyramid with a mean Zr–O distance of 0.213 nm. Two of the ZrO_7 polyhedra mutually share edges, and they are connected through PO_4 polyhedra to form infinite chains parallel to [001]. Individual chains are linked together, resulting in the formation of a two-dimensional sheet parallel to (100). These sheets are stacked in the [100] direction, and they are linked through the strontium atoms to form a three-dimensional structure. Two other polymorphic forms were confirmed at high temperatures up to 1473 K; the crystal underwent the phase transitions from triclinic to monoclinic at 405 K, then to hexagonal (or trigonal) at 1196 K during heating. The monoclinic phase is most probably isostructural with yavapaiite. The higher- and lower-temperature polymorphs of the yavapaiite-type structure have been described for the first time.

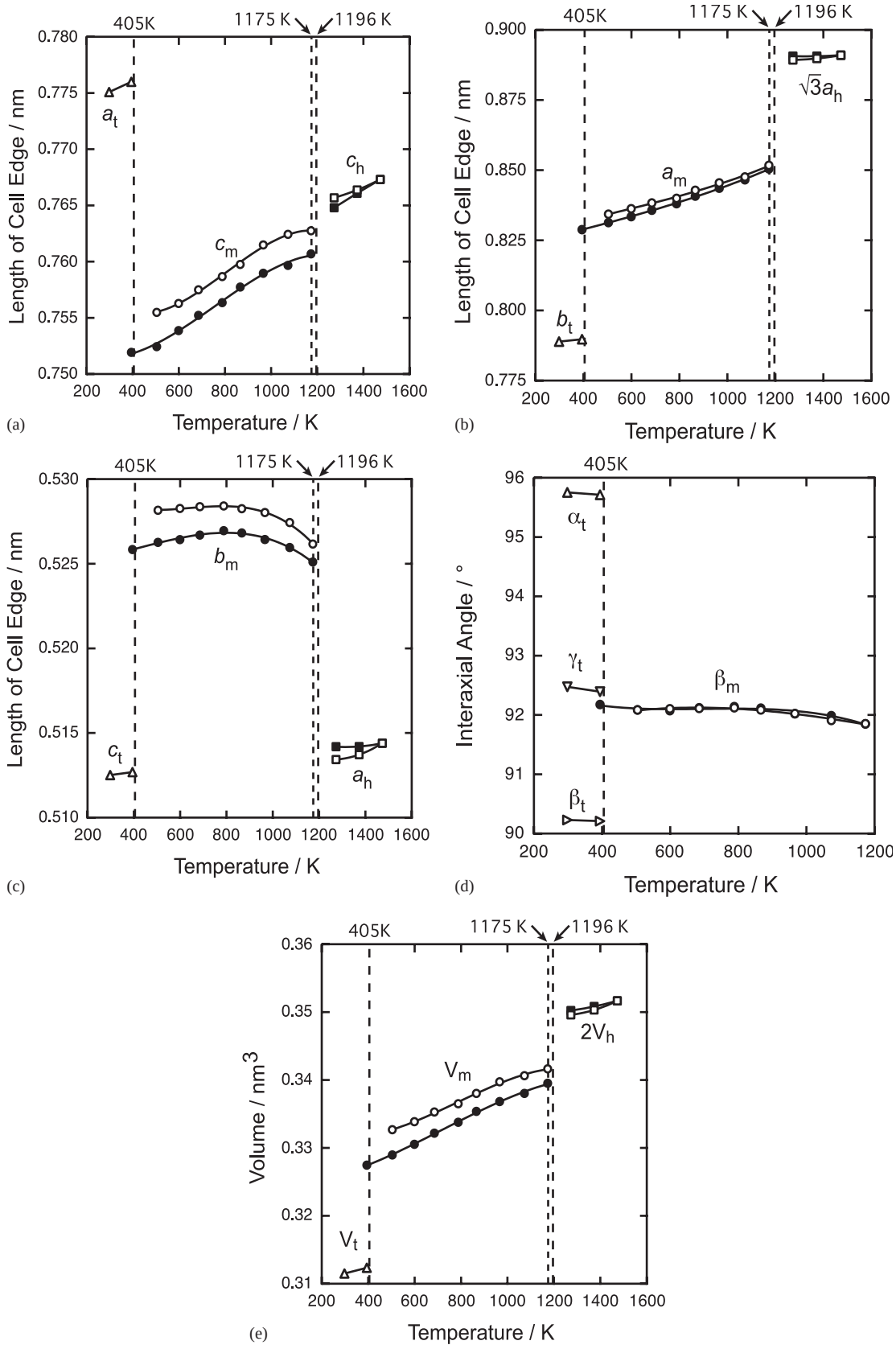

Fig. 6. Variation of cell parameters with temperature. (a) a_t, c_m, and c_h, (b) b_t, a_m, and $\sqrt{3}a_h$, (c) c_t, b_m, and a_h, (d) α_t, β_t, γ_t, and β_m, and (e) V_t, V_m and $2V_h$. During heating, the successive phase transitions from (open triangle) triclinic to (open circle) monoclinic, then to (open square) hexagonal (or trigonal) occur at, respectively, 405 and 1196 K. Upon cooling, the reverse phase transition from (closed square) hexagonal to (closed circle) monoclinic occurs at 1175 K. The subsequent monoclinic-to-triclinic phase transition is incomplete, with the coexistence of both phases below 394 K.

References

[1] M.Th. Paques-Ledent, J. Inorg. Nucl. Chem. 39 (1977) 11–17.
[2] R. Masse, A. Durif, C. R. Seances Acad. Sci. Ser. C 274 (1972) 1692–1695.
[3] M. Kinoshita, M. Inoue, Nippon Kagaku Kaishi 8 (1980) 1219–1223.
[4] M. Kinoshita, M. Inoue, Nippon Kagaku Kaishi 9 (1982) 1473–1478.
[5] M. Sakurai, F. Tsuchiya, H. Suzuki, M. Maeda, M. Watanabe, Phosphorus Res. Bull. 12 (2001) 117–122.
[6] K. Fukuda, K. Fukutani, Powder Diffr. 18 (2003) 296–300.
[7] C. Dong, J. Appl. Crystallogr. 32 (1999) 838.
[8] P.E. Werner, L. Eriksson, M. Westdahl, J. Appl. Crystallogr. 18 (1985) 367–370.
[9] P.M. de Wolff, J. Appl. Crystallogr. 1 (1968) 108–113.
[10] G.S. Smith, R.L. Snyder, J. Appl. Crystallogr. 12 (1979) 60–65.
[11] G.S. Pawley, J. Appl. Crystallogr. 14 (1981) 357–361.
[12] H. Toraya, J. Appl. Crystallogr. 19 (1986) 440–447.
[13] C.R. Hubbard, J. Appl. Crystallogr. 16 (1983) 285–288.
[14] A. Altomare, M.C. Burla, M. Camalli, B. Carrozzini, G.L. Cascarano, C. Giacovazzo, A. Guagliardi, A.G.G. Moliterni, G. Polidori, R. Rizzi, J. Appl. Crystallogr. 32 (1999) 339–340.
[15] R.A. Young, in: R.A. Young (Ed.), The Rietveld Method, Oxford University Press, Oxford, UK, 1993, pp. 1–38.
[16] F. Izumi, in: R.A. Young (Ed.), The Rietveld Method, Oxford University Press, Oxford, UK, 1993, pp. 236–253.
[17] H. Toraya, J. Appl. Crystallogr. 23 (1990) 485–491.
[18] W.A. Dollase, J. Appl. Crystallogr. 19 (1986) 267–272.
[19] R.O. Simmons, J. Appl. Phys. 41 (1970) 2235–2240.
[20] I.D. Brown, D. Altermatt, Acta Crystallogr. B 41 (1985) 244–247.
[21] N.E. Brese, M. O'Keeffe, Acta Crystallogr. B 47 (1991) 192–197.
[22] T. Balic-Zunic, I. Vickovic, Acta Crystallogr. 29 (1996) 305–306.
[23] D.W.J. Cruickshank, Acta Crystallogr. 17 (1964) 671–672.
[24] W. Gebert, E. Tillmanns, Acta Crystallogr. B 31 (1975) 1768–1770.
[25] E. Makovicky, T. Balic-Zunic, Acta Crystallogr. B 54 (1998) 766–773.
[26] N. Penin, L. Seguin, M. Touboul, G. Nowogrocki, Int. J. Inorg. Mater. 3 (2001) 1015–1023.
[27] R.D. Shannon, Acta Crystallogr. A 32 (1976) 751–767.
[28] J.W. Christian, The Theory of Transformations in Metals and Alloys, 2nd Edition, Pergamon Press, Oxford, 1975, pp. 12–14.
[29] G.L. Nord, in: P.R. Buseck (Ed.), Minerals and Reactions at the Atomic Scale: Transmission Electron Microscopy, Mineralogical Society of America, Washington, DC, 1992, pp. 455–508.